Gong *et al. Biochar* (2026) 8:120
https://doi.org/10.1007/s42773-026-00642-8

Biochar

ORIGINAL RESEARCH Open Access

Promoted sequestration and photo-induced destruction of perfluorooctane sulfonate using photoregenerable β-Ga_2O_3-functionalized biochar: superior defluorination and mechanistic insights

Yanyan Gong[1*], Dongjiao Lin[1], Ying Liu[1], Shuai Gao[2], Haodong Ji[2], Lianjun Bao[1], Zuhui Wu[1], Honghong Lyu[3] and Dongye Zhao[4*]

Abstract

The unique presence of perfluorooctane sulfonate (PFOS) in aquatic matrices has intensified the urgent demand for economically viable remediation technologies to comply with the stringent regulations. To address this challenge, we developed a novel β-Ga_2O_3-functionalized biochar adsorptive photocatalyst (Ga_2O_3@biochar) for successive sequestration and photocatalytic destruction of PFOS in both lab water and real groundwater. The composite material loaded with 1% Ga demonstrated the best performance. The incorporation of β-Ga_2O_3 into the porous structure of the biochar matrix modulated its physicochemical and optoelectronic properties, resulting in enhanced mesoporosity for improved PFOS mass transfer and adsorption, improved light absorption, a narrower bandgap, and better charge separation. Density functional theory (DFT) calculations corroborated an efficient interfacial electron transfer from biochar to β-Ga_2O_3. The composite exhibited exceptional PFOS adsorption due to concurrent hydrogen bonding, hydrophobic interaction, mesopore filling, and electrostatic attractions. Following the pre-adsorption, the material was able to photodegrade 80.8% of the pre-loaded PFOS, with 70.5% defluorinated, and the degradation process was accurately described by a delayed first-order kinetic equation. Photogenerated electrons (e^-), superoxide radicals ($\cdot O_2^-$), and singlet oxygen ($^1O_2$) acted as the predominant reactive species, contributing 35.0%, 39.1%, and 25.8% to the overall PFOS degradation, respectively. The PFOS degradation proceeded via a chain-shortening pathway initiated by desulfonation, followed by decarboxylation and a series of defluorination. The photodegradation regenerated the composite, allowing for reuse in multiple adsorption–photodegradation cycles. Moreover, the composite performed effectively in real groundwater. Overall, the new material appeared promising and may enable the concentrate-&-destroy strategy for treating PFOS and likely other PFAS in water.

*Correspondence:
Yanyan Gong
yanyangong@jnu.edu.cn
Dongye Zhao
dzhao2@sdsu.edu
Full list of author information is available at the end of the article

Springer

Highlights

- Novel adsorptive photocatalyst Ga_2O_3@biochar achieved >99% adsorption and 80.8% degradation with superior 70.5% defluorination.
- DFT verifies electron transfer from biochar to β-Ga_2O_3 for charge separation.
- e^-, $\cdot O_2^-$, and $^1O_2$ contribute 35.0%, 39.1%, and 25.8% to stepwise chain-shortening mineralization.
- Ga_2O_3@biochar enables concentrate-&-destroy of PFOS and performs effectively in reuse cycles and real groundwater.

Keywords PFAS, PFOS, Biochar, Catalyst, Adsorption, Photodegradation

Graphical Abstract

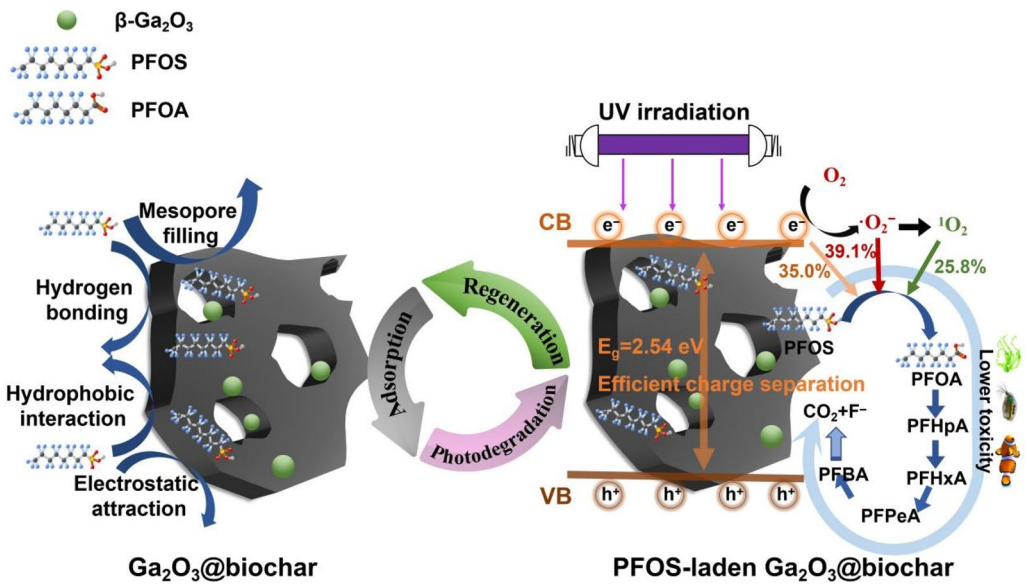

1 Introduction

Per- and polyfluoroalkyl substances (PFAS) constitute a diverse group of synthetic aliphatic molecules where the hydrogen atoms on the carbon backbone are partially or entirely replaced by fluorine atoms (Gagliano et al. 2020). Due to their extremely strong C–F bond energy (536 kJ mol^{-1}), strong thermal and chemical stability, and extensive applications, PFAS have been ubiquitously detected in aquatic systems (Barzen-Hanson et al. 2017; Li et al. 2020). As one of the most prevalent legacy PFAS, perfluorooctane sulfonate (PFOS) has been under close scrutiny due to its widespread detection in drinking water, surface waters, and groundwater with concentrations ranging from a few ng L^{-1} to tens of μg L^{-1} (Loos et al. 2009; Xiao et al. 2015; Wee and Aris. 2023). Chronic exposure to PFOS has been linked to severe physiological dysfunctions including thyroid hormone disruption, immune system impairment, liver damage, and carcinogenic risks (Habib et al. 2024). In response, regulatory limits for PFOS in drinking water have been established worldwide. For example, the United States Environmental Protection Agency has set an legally enforceable maximum contaminant level of 4 ng L^{-1} for PFOS (USEPA 2025), and China has promulgated a national standard of 40 ng L^{-1} (GB 5749-2022). Consequently, cost-effective technologies have been intensively sought in recent years to help the tens of thousands of affected water utilities to comply with the stringent regulations.

In aquatic environments, PFOS typically exists in anionic forms ($pK_a \approx -3.27$) (Wang and Shih. 2011). Adsorption has been one of the most reported approaches for removal of PFAS including PFOS owing to its operation simplicity and cost-effectiveness. Commonly used adsorbents include activated carbon, anion exchange resins, mineral materials, and biomaterials (Du et al.

2014). Among them, biochar, a carbon-abundant and highly conjugated solid matrix derived from the thermos-chemical conversion of biomass under oxygen-deficient or anoxic environments, presents a promising alternative to activated carbon due to its low-cost and abundant precursor feedstocks (Ramos and Ashworth. 2024). For example, Zhang et al. (2023) synthesized an acid-modified biochar derived from sludge and found that the adsorbent was able to effectively remove PFOS from water via concurrent electrostatic interactions, hydrogen bonding, and hydrophobic interaction. However, practical application of adsorption for PFAS has been limited by some key drawbacks, including (1) the fact that adsorption only physically separates and concentrates PFOS without degradation, and (2) the fact that regeneration of saturated adsorbents typically consumes expensive and noxious organic media (e.g., ethanol and methanol) and/or NaOH, which is not only costly but generates secondary waste residual needing further handling and disposal (Xu et al. 2020).

In recent years, photocatalysis of PFAS has drawn growing interest for its ability to degrade or mineralize PFAS under moderate conditions (Zhu et al. 2026). To this end, various semiconductors based on TiO_2, Ga_2O_3, In_2O_3, ZnO, and Bi_2O_3 have been widely tested as photocatalysts (Liu et al. 2022). β-Ga_2O_3 stands out as one of the most effective photocatalyst due to its strong redox potential associated with its wide bandgap energy (4.8 eV) and high chemical stability (Wei et al. 2017). For instance, Fu et al. (2022a) tested five photocatalysts for PFOA photodegradation and ranked the materials as follows: $Ga_2O_3 > TiO_2 > CeO_2 > In_2O_3 >$ CdS in terms of PFOA degraded in 10 h at pH 3.0. Ga_2O_3 is also environmentally benign according to the Worksafe Australia criteria. Nevertheless, neat β-Ga_2O_3 is constrained by its limited light absorption and poor ability to separate the photogenerated electron and holes (Zhang et al. 2019).

In addition, it is impractical to directly treat vast quantities of bulk water harboring trace levels of PFOS using traditional photocatalysts. To address this challenge, a novel concentrate-&-destroy strategy has emerged as a promising alternative. This approach employs composite materials that synergistically integrate adsorption and photodegradation, namely, trace levels of PFAS are first concentrated from a large volume of water onto a small amount of adsorptive photocatalyst, and then degraded by localized photocatalysis under light irradiation (Li et al. 2020). For instance, a study by Zhu et al. (2021) reported that gallium-doped carbon-modified titanate nanotubes exhibited accelerated adsorption kinetics and heightened affinity for PFOS compared to pristine-activated carbon, and achieved 75.0% degradation and 66.2% mineralization efficiencies under 4 h of UV exposure. Despite these advances, several challenges are yet to be overcome for further advancement of this strategy, including (1) relatively complex and costly material synthesis, (2) relatively low degradation and, in particular, mineralization efficiencies, and (3) insufficient evaluation of adsorptive photocatalyst performance under real water matrix conditions.

Beyond serving as an efficient adsorbent for PFOS, biochar itself may exhibit photoactive properties. The presence of persistent free radicals and quinone moieties within the biochar framework can trigger the generation of reactive oxygen species (ROS) upon photoexcitation, leading to the oxidative transformation of adsorbed organic contaminants (Luo et al. 2021). In our prior work, we prepared an engineered biochar via NaOH-modification and calcination, and the material demonstrated excellent adsorption capability for PFOS, though its degradation performance was limited (Lin et al. 2025). While various adsorption-photocatalysis composites have been developed to address such limitations, existing systems frequently suffer from pore blockage that hinders the mass transfer of bulky PFAS molecules, inefficient interfacial electron transfer, and low defluorination efficiencies. Distinct from conventional composites and inspired by the concentrate-&-destroy strategy, we hypothesize that a rationally designed Ga_2O_3-modified biochar heterojunction can overcome these inherent bottlenecks. Specifically, we anticipate that the chemical integration will not only trigger targeted mesopore evolution to accommodate PFOS molecules, but also induce an interfacial electronic modulation. This synergy is expected to simultaneously enhance the material's adsorption capacity and affinity, improve its light-harvesting capability, promote the separation efficiency of photogenerated carriers, and ultimately achieve superior PFOS photodegradation and defluorination while enabling entirely chemical-free regeneration.

The overall goal of this study was to synthesize, characterize, and evaluate a novel Ga_2O_3-modified biochar composite (Ga_2O_3@biochar) for synergistic sequestration and subsequent photocatalytic degradation of PFOS in aqueous environments. The specific objectives were to (1) synthesize the bifunctional catalyst via a two-step hydrothermal-calcination protocol; (2) test its adsorption kinetics and capacity towards PFOS; (3) assess the photodegradation and mineralization effectiveness of pre-concentrated PFOS; (4) elucidate the fundamental mechanisms governing the enhanced adsorption and photocatalytic activity through comprehensive material characterization and density functional theory (DFT) calculations; (5) identify the degradation pathways and assess the toxicity of intermediates; (6) assess the

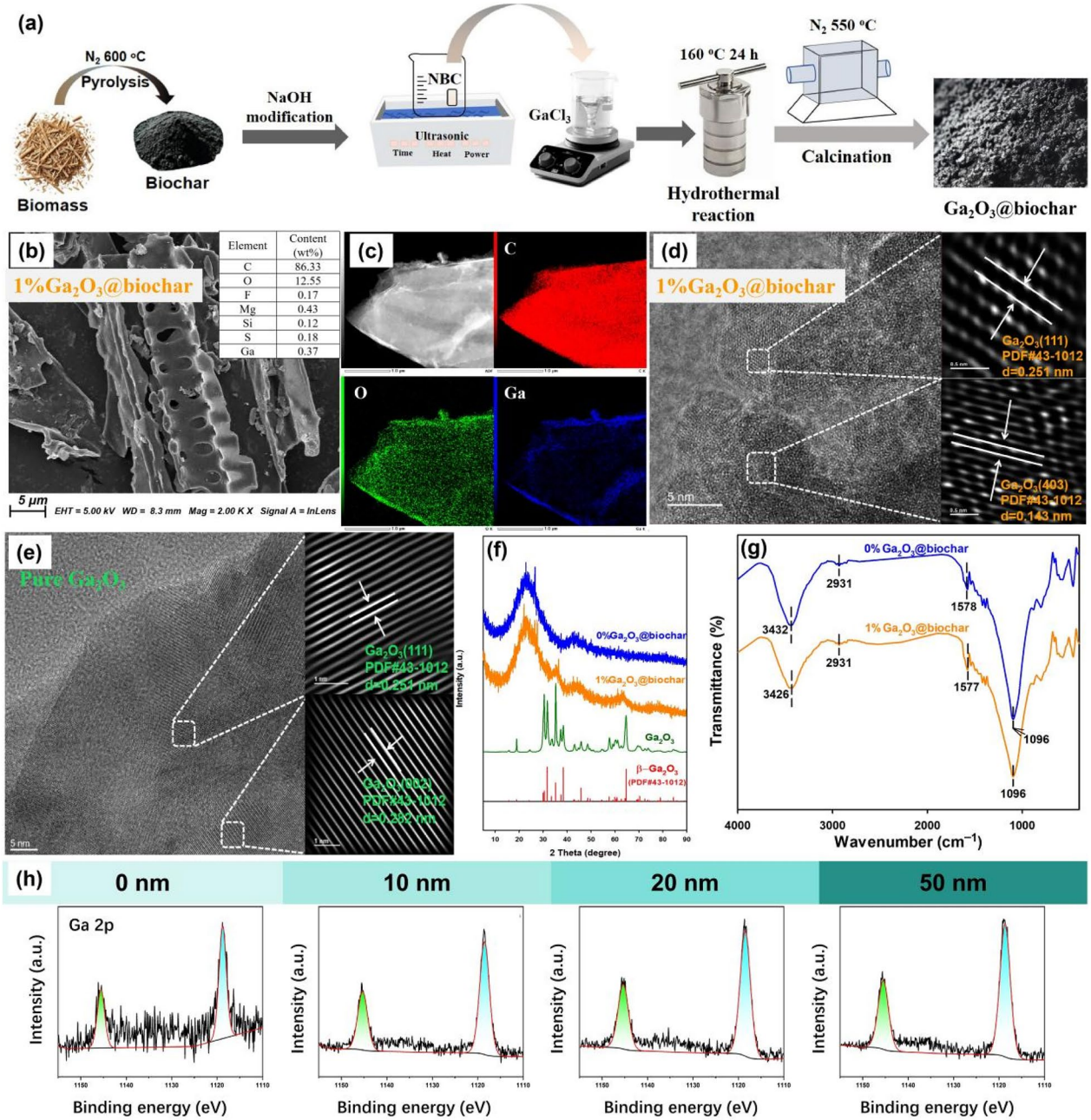

Fig. 1 Synthesis and characterizations of Ga_2O_3@biochar. **a** Schematic of material preparation, **b** SEM–EDS images of 1%Ga_2O_3@biochar, **c** TEM images and elemental mapping, **d** HRTEM images of 1%Ga_2O_3@biochar, **e** HRTEM images and pure Ga_2O_3, **f** XRD, **g** FTIR, and **h** Ga 2p XPS depth profiling spectra

material's reusability and stability; and (7) examine its performance using a model real groundwater.

2 Materials and methods

2.1 Materials and chemicals

All chemical reagents utilized throughout this investigation were of analytical grade or higher, with comprehensive specification provided in Text S1 in the Supplementary Information (SI).

2.2 Preparation of Ga_2O_3@biochar

Ga_2O_3@biochar was synthesized via a two-step hydrothermal and calcination approach (Fig. 1a). Briefly, biochar was initially produced by pyrolyzing ~1 g of wheat

straw (600 °C, 2 h) under a continuous N_2 flow. The prepared biochar underwent alkaline activation in 50 mL of 0.1 M NaOH for 24h. The solids were separated via centrifugation and then washed batchwise with deionized (DI) water until the supernatant achieved a neutral pH, followed by oven-drying at 105 °C for 12 h. A 0.5 g portion of the treated biochar was then homogenized in 1:1 (v/v) water/methanol co-solvent (40 mL total) via 1 h of sonication. Following this, 20 mL of a $GaCl_3$ solution at various concentrations (0–3.16 g L^{-1}) was introduced under continuous stirring. After 1 h, the suspension was sealed into a Teflon-lined stainless-steel vessel for a 24-h hydrothermal reaction at 160 °C. The solids were collected, washed with DI water to achieve neutral pH, and oven-dried at 60 °C. Finally, the dried solid was calcinated at 550 °C for 3 h. Given the Ga mass loading, the obtained composite was identified as 0%Ga_2O_3@biochar, 0.5%Ga_2O_3@biochar, 1%Ga_2O_3@biochar, 2%Ga_2O_3@biochar, 3%Ga_2O_3@biochar, and 5%Ga_2O_3@biochar.

2.3 Material characterization

The microscopic architecture and elemental distributions were visualized using scanning electron microscopy (SEM) integrated with energy disperse spectroscopy (EDS), high-resolution transmission electron microscopy (HRTEM), and elemental mapping. The crystallographic phases and surface functional groups were identified by X-ray diffraction (XRD) and Fourier transform infrared spectroscopy (FTIR). The hydrophobicity was evaluated via water contact angle measurement and the surface charge was determined using a Zetasizer instrument. The specific surface area and pore structure were obtained from N_2-adsorption/desorption isotherms. The elemental valence states and chemical environments were explored by X-ray photoelectron spectroscopy (XPS) with depth profiling. For optoelectronic characterization, UV–vis diffuse reflectance spectra (UV–vis DRS) and photoluminescence (PL) were recorded. Furthermore, electrochemical behaviors including cyclic voltammetry (CV) and electrochemical impedance spectroscopy (EIS) were explored. Detailed instrument specifications and operational parameters are provided in Text S2.

2.4 Theoretical calculations

The interfacial structure and charge transfer mechanisms were further investigated via the first-principle calculations per the density functional theory (DFT). The calculations were performed with the Vienna Ab initio Simulation Package (VASP). The PBE (Perdew–Burke–Ernzerhof) functional within the Generalized Gradient Approximation (GGA) framework were employed to describe the exchange–correlation interactions (Perdew et al. 1996), with van der Waals forces corrected by the Grimme D3 scheme. A 500 eV plane-wave energy cutoff was used, and structural relaxations continued until energy converged to 10^{-5} eV, with residual forces under 0.05 eV $Å^{-1}$. A Ga_2O_3(112)/biochar heterojunction was constructed based on the HRTEM data to study interfacial charge transfer.

2.5 Adsorption of aqueous PFOS using Ga_2O_3@biochar

The adsorption performance of various biochar-based materials towards PFOS was evaluated through systematic batch experiments. The batch adsorption equilibrium tests were initiated by introducing 0.05 g L^{-1} of each adsorbent in a suspension containing 100 μg L^{-1} PFOS in 40 mL polypropylene centrifuge tubes. The pH was maintained at 7.0 ± 0.3. The mixtures were agitated on a rotator at 40 rpm for 24 h to reach equilibrium. The solids were separated via centrifugation (4000 rpm, 2 min) and the resulting supernatants were filtrated through 0.22-μm polypropylene syringe filters prior to analysis. Control experiments followed the same protocol but omitted the addition of adsorbents.

Adsorption kinetics and isotherms were investigated for 0%Ga_2O_3@biochar and 1%Ga_2O_3@biochar following similar procedures. For kinetic studies, the samples were collected at predetermined time intervals. For isotherm studies, initial PFOS levels were adjusted across a range of 0–1.5 mg L^{-1} (specifically, 0, 40, 70, 100, 200, 300, 500, 700, 1000, and 1500 μg L^{-1}) utilizing a fixed adsorbent loading of 0.10 g L^{-1}. All experiments were performed in triplicate.

2.6 Photodegradation of pre-concentrated PFOS

Upon reaching adsorption equilibrium (initial PFOS concentration of 100 μg L^{-1} and adsorbent dosage of 0.15 g L^{-1}), the suspension underwent centrifugation at 4000 rpm for 2 min. 90% of the aqueous phase was discarded. The residual slurry was subsequently transferred into a quartz-lidded petri dish and diluted to 10 mL with ultrapure water. Throughout the experiment, the pH was stabilized at 7.0 ± 0.3. Dark control experiments demonstrated that the leaching of adsorbed PFOS back into the aqueous phase was negligible (<3%), ensuring the stability of the pre-concentrated phase. Photodegradation was initiated by exposing the sample to a UV light source (254 nm, 30.0 mW cm^{-2}) at 23 ± 2 °C, with intermittent manual agitation performed hourly. After 8 h, the mixture underwent centrifugation to harvest the supernatant for quantification of PFOS and fluoride. In addition, the solid-bound PFOS was extracted using methanol (40 mL) at 70 °C for a duration of 4 h. Utilizing M8PFOS as the recovery standard, the overall mass recovery was validated to be between 90% and 100%. The PFOS

photodegradation efficiency was calculated according to the following equation:

$$\text{Photodegradation} \cdot \text{efficiency}(\%) = \frac{\text{PFOS}_{\text{adsorbed}} - \text{PFOS}_{\text{supernatant}} - \text{PFOS}_{\text{extracted}}}{\text{PFOS}_{\text{adsorbed}}} \times 100 \quad (1)$$

where $\text{PFOS}_{\text{adsorbed}}$ represents the mass of PFOS adsorbed after the adsorption tests, $\text{PFOS}_{\text{supernatant}}$ refers to the mass of PFOS in the supernatant after photodegradation, and $\text{PFOS}_{\text{extracted}}$ is the mass of PFOS recovered from the solid phase after photodegradation. Defluorination efficiency was determined based on the fluoride concentration measured in the aqueous phase. To ensure the accuracy of this quantification, several control experiments were performed: First, no fluoride was detected in either pure PFOS solution or 1%Ga_2O_3@biochar suspension alone, ruling out background fluoride. Second, independent F^- adsorption tests revealed that the composite possessed negligible fluoride adsorption, ensuring that the photogenerated F^- remained entirely in the aqueous phase. Consequently, the measured aqueous F^- concentration served as an accurate indicator of C–F bond cleavage.

To elucidate the ROS participating in the photocatalytic degradation, quenching experiments were performed using various scavengers, including EDTA-2Na for photogenerated holes (h^+), silver nitrate ($AgNO_3$) for photogenerated electrons (e^-), isopropyl alcohol (IPA) for hydroxyl radicals (·OH), furfuryl alcohol (FFA) for singlet oxygen ($^1O_2$), and benzoquinone (BQ) for superoxide radicals ($\cdot O_2^-$). Moreover, electron spin resonance (ESR) spectroscopy (EMXplus, Bruker, Karlsruhe, Germany) was conducted to verify ROS formation, using DMPO for ·OH and $^1O_2$ detection and TEMP for $^1O_2$ detection.

2.7 Reusability of Ga_2O_3@biochar

To assess the reusability of Ga_2O_3@biochar, four consecutive adsorption-photodegradation cycles were carried out. In each cycle, adsorption was initiated using 100 μg L^{-1} of PFOS with an adsorbent loading of 0.80 g L^{-1} in 40 mL solution at pH 7.0 ± 0.3. Following a 24 h equilibration period (Sect. 2.5), the pollutant-laden matrix was then harvested for subsequent photodegradation (Sect. 2.6). After irradiation, the photo-regenerated adsorbent was recovered and reused in subsequent adsorption step.

2.8 Concentration and destruction of PFOS in field groundwater using Ga_2O_3@biochar

A groundwater sample was collected from a well near a landfill site in Guangzhou, China. The latitude/longitude of the sampling site was 23.27/113.49. The sample was filtered through a 0.22-μm polypropylene membrane filter to remove suspended solids and the filtrate was analyzed for basic physicochemical properties. The original PFOS concentration was below 300 ng L^{-1}. To facilitate the subsequent PFOS removal tests, the groundwater sample was spiked with 100 μg L^{-1} PFOS. Adsorption and photodegradation experiments were performed as outlined in Sects. 2.5 and 2.6.

2.9 Analytical methods

PFOS and M8PFOS were quantified using a Shimadzu ultra-high-performance liquid chromatography (UHPLC) system integrated with an AB-Sciex 5500 triple quadrupole mass spectrometer. The established limits of detection were 300 ng L^{-1} and 0.4 ng L^{-1}, respectively (refer to Text S3 for comprehensive methodology). Aqueous F^- was determined via Dionex ICS-5000 DC ion chromatograph (Thermo Scientific, CA, USA) with a detection limit of 7.5 μg L^{-1}. Aqueous Ga was quantified on PerkinElmer NexION 350S ICP-MS (Waltham, MA, USA), achieving a sensitivity of 0.2 μg L^{-1}.

3 Results and discussion

3.1 Physicochemical properties of Ga_2O_3@biochar

The Ga content in the composite was determined to be 0.5%, 1.0%, 1.98%, 3.19%, and 4.65%, respectively, for 0.5%Ga_2O_3@biochar, 1%Ga_2O_3@biochar, 2%Ga_2O_3@biochar, 3%Ga_2O_3@biochar, and 5%Ga_2O_3@biochar, indicating that Ga was successfully loaded on biochar.

Figure S1 and Fig. 1b show the morphological feature and chemical composition of 0%Ga_2O_3@biochar and 1%Ga_2O_3@biochar, respectively. Both materials retained the inherent longitudinal structure of wheat straw and exhibited porous tubular structures with well-developed pores (Liu et al. 2025), leading to high specific surface areas (409.06 m^2 g^{-1} for 0%Ga_2O_3@biochar and 276.71 m^2 g^{-1} for 1%Ga_2O_3@biochar) (Table S1). Such a texture is advantageous for catalytic applications as it provides abundant active sites and enhances light harvesting via multiple internal reflection with scattering (Gonzalez-Gonzalez et al. 2022). Ga_2O_3 particles were dispersed on the biochar surface (Fig. 1b). The EDS analysis revealed the presence of C and O as major elements, along with trace amounts of F, Mg, Si, and S in both materials. Characteristic Ga signal was exclusively identified in 1%Ga_2O_3@biochar (Fig. 1b), further verifying the incorporation of Ga. It is noteworthy that the EDS gave a Ga content of 0.37% for 1%Ga_2O_3@biochar, which was lower than the expected 1.0 wt%. The discrepancy can be attributed to the fact that EDS analysis only provides localized surface elemental composition rather than the overall bulk content (Ruiz-Vargas et al. 2014).

In addition, irregularly shaped Ga_2O_3 aggregates were observed on 1%Ga_2O_3@biochar (Fig. 1c). The elemental mappings indicated a non-uniform distribution of Ga on 1%Ga_2O_3@biochar. Further HRTEM (Fig. 1d) revealed distinct lattice fringes with spacing of 0.251 nm and 0.143 nm, corresponding to the (111) and (403) crystallographic planes of β-Ga_2O_3, respectively.

The specific surface area and pore structure were investigated via the N_2 adsorption–desorption technique (Fig. S2; Table S1). The isotherms for both 0%Ga_2O_3@biochar and 1%Ga_2O_3@biochar exhibited type I (sharp uptake at low pressure P/P_0, indicative of micropores) and type IV (hysteresis loop at medium P/P_0, representative of mesopores) features, confirming a hierarchical micro-mesoporous architecture. The 0%Ga_2O_3@biochar possessed a high specific surface area (409.1 $m^2\ g^{-1}$), predominantly associated with its significant micropore area (334.9 $m^2\ g^{-1}$) and micropore volume (0.13 $cm^3\ g^{-1}$). The average pore size was 5.37 nm. Following Ga doping, 1%Ga_2O_3@biochar showed a noticeable reduction in specific surface area (276.7 $m^2\ g^{-1}$), micropore area (182.6 $m^2\ g^{-1}$), and micropore volume (0.08 $cm^3\ g^{-1}$), while a slight increase of the average pore size to 5.75 nm. The mesopore volume was increased from 0.10 $cm^3\ g^{-1}$ for 0%Ga_2O_3@biochar to 0.15 $cm^3\ g^{-1}$ for 1%Ga_2O_3@biochar. These results indicate that the deposition of Ga_2O_3 on biochar blocked some of the micropores or passage to the micropores. On the other hand, new mesopores could be formed in the porous structure of the deposited Ga_2O_3 on the biochar surface. Moreover, the presence of Ga_2O_3 could promote the volatilization and cracking of volatiles and tar within the biochar (Jia et al. 2021), further modulating the pore structure. The increased mesoporosity was advantageous for enhancing the mass transfer of PFOS (the molecular dimension of PFOS was approximately 1.32 nm (Du et al. 2016)).

The crystalline nature of 0%Ga_2O_3@biochar and 1%Ga_2O_3@biochar were examined using XRD, as shown in Fig. 1f. 0%Ga_2O_3@biochar exhibited two distinct peaks at 22.9° and 43.5°, corresponding to the (002) plane of amorphous carbon and the (100) plane of crystalline graphite, respectively (Wang et al. 2022; Yu et al. 2023). Pure Ga_2O_3 displayed diffraction signals at 30.2°, 31.7°, 35.2°, 37.4°, 38.4° and 70.3° corresponding to the (−401), (002), (111), (401), (−311), and (022) planes of β-Ga_2O_3 (PDF#43-1012). Upon Ga loading, two characteristic diffraction peaks at 35.4° and 64.5° appeared, which were assigned to the (111) and (512) planes of β-Ga_2O_3 (PDF#43-1012) (Pan et al. 2025), confirming that Ga was predominantly present in the form of β-Ga_2O_3 in 1%Ga_2O_3@biochar. Figure 1g shows the FTIR spectra. 0%Ga_2O_3@biochar featured four characteristic peaks at 3432 cm^{-1} (O–H stretching), 2931 cm^{-1} (C–H stretching), 1578 cm^{-1} (C=O stretching), and 1096 cm^{-1} (C–O stretching). The Ga doping did not alter the type of functional groups. Yet, the O–H and C=O stretching peaks shifted to 3426 and 1577 cm^{-1}, respectively. Additionally, the intensities of the O–H and C–O bands decreased. These changes are probably attributed to the interactions between Ga and oxygen-containing functional groups on the biochar surface.

XPS depth profiling was performed to further elucidate the chemical composition and spatial distribution of 1%Ga_2O_3@biochar (Fig. 1h; Fig. S3). The C 1s spectra exhibited three distinct peaks at 288.8, 286.6, and 284.8 eV, representing O–C=O (Zhang et al. 2023), C–O (Zhang et al. 2021b), and C–C/C=C (Zhang et al. 2023), respectively. The O 1s spectrum was deconvoluted into three peaks at 533.5, 532.1, and 530.8 eV, which were attributed to O–C=O (Zhang et al. 2023), –OH (Su et al. 2024), and C=O (Fu et al. 2022b), respectively. For Ga 2p spectra, two characteristic peaks were observed at 1118.8 eV (Ga $2p_{3/2}$) and 1145.6 eV (Ga $2p_{1/2}$), respectively, confirming the presence of Ga in the composite. It should be noted that Ga was detected from the outermost surface to a sputter depth of 50 nm, providing direct evidence that Ga was incorporated not only on the external surface but also within the interior pore structure of biochar.

3.2 Optical properties and interfacial characteristics of Ga_2O_3@biochar

Figure 2a shows the UV–vis DRS data. It is evident that 1%Ga_2O_3@biochar exhibited a redshift in the absorption edge and enhanced light absorption compared to 0%Ga_2O_3@biochar. The corresponding bandgap energies derived from the Tauc plot were 4.54 eV for pure Ga_2O_3, 2.91 eV for 0%Ga_2O_3@biochar, and 2.54 eV for 1%Ga_2O_3@biochar. The reduced bandgap of the composite facilitated improved light harvesting and charge carrier generation, thereby enhancing its photocatalytic activity (Meng et al. 2020).

PL spectra was employed to probe the separation and recombination of photogenerated carriers (Fig. 2b). Generally, the higher the fluorescence intensity, the higher the recombination efficiency. 1%Ga_2O_3@biochar demonstrated lower fluorescence intensity, indicating suppressed recombination of photogenerated electron–hole pairs. This phenomenon was attributed to modified spatial distribution of the charger carriers induced by the interactions between Ga and functional groups of biochar (Lv et al. 2024). Notably, 1%Ga_2O_3@biochar exhibited three distinct blue-light emission peaks at 409 nm (~2.99 eV), 433 nm (~2.83 eV), and 470 nm (~2.70 eV),

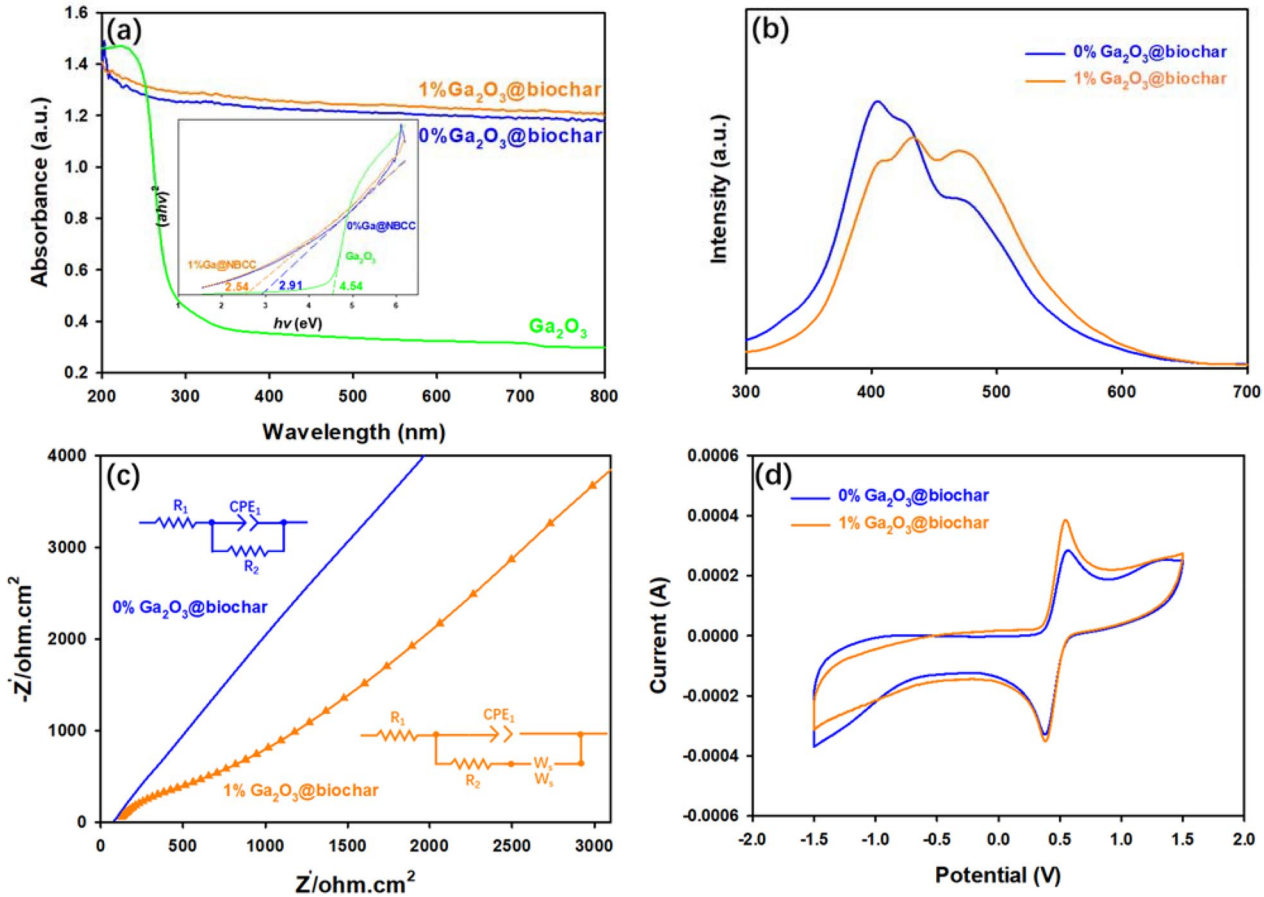

Fig. 2 Optical and electrochemical characteristics of 0%Ga_2O_3@biochar and 1%Ga_2O_3@biochar. **a** UV–vis DRS spectra (inset shows corresponding Tauc plot), **b** PL spectra, **c** EIS spectra, and **d** CV curves

characteristic of Ga_2O_3 (Zhang et al. 2004). During the preparation of 1%Ga_2O_3@biochar, a number of oxygen vacancies or gallium–oxygen vacancy pairs can be produced (Zhang et al. 2004). Under 254 nm UV irradiation, electrons are excited from the valence band (VB) to the conduction band (CB). The electrons move freely within the CB and subsequently relax into the donor band associated with oxygen vacancies. The recombination of the electrons in the donor band with the acceptors formed by gallium-oxygen vacancy pairs results in the blue emission centered at 433 nm (Zhang et al. 2005).

Figure 2c shows that the EIS spectrum of 0%Ga_2O_3@biochar was nearly linear, with the charge transfer resistance (R_{ct}) determined to be 73,254 Ω. In contrast, 1%Ga_2O_3@biochar displayed a significantly smaller arc radius and a 107-fold lower R_{ct} (683.4 Ω), indicating an enhanced separation and transfer of photogenerated electron–hole pairs (Pan et al. 2025). The Warburg impedance feature for 1%Ga_2O_3@biochar at low frequencies further corroborated the efficient charge diffusion to surface reaction sites. Furthermore, the CV curves (Fig. 2d) confirmed superior charge storage capability in 1%Ga_2O_3@biochar, evidenced by its larger integrated CV area (Wang et al. 2024).

DFT-based calculations were performed to investigate the charge distribution at the heterojunction interface between Ga_2O_3 and biochar. The results showed a higher work function for Ga_2O_3 (6.02 eV) than that for biochar (4.23 eV), suggesting that the electrons transferred from biochar to Ga_2O_3 (Fig. 3a, b). Meanwhile, the charge distribution of 1%Ga_2O_3@biochar (Fig. 3c, d) demonstrated electron depletion in biochar and accumulation in Ga_2O_3.

Taken together, the incorporation of β-Ga_2O_3 into the biochar matrix improved light absorption, reduced bandgap, and facilitated charger carrier separation by optimized electronic properties, thereby enhancing the catalytic activity and facilitating the ROS production.

3.3 Effects of Ga content on PFOS adsorption and photodegradation

Figure 4 compares the equilibrium uptake of PFOS by Ga_2O_3@biochar at various Ga contents. Pure Ga_2O_3

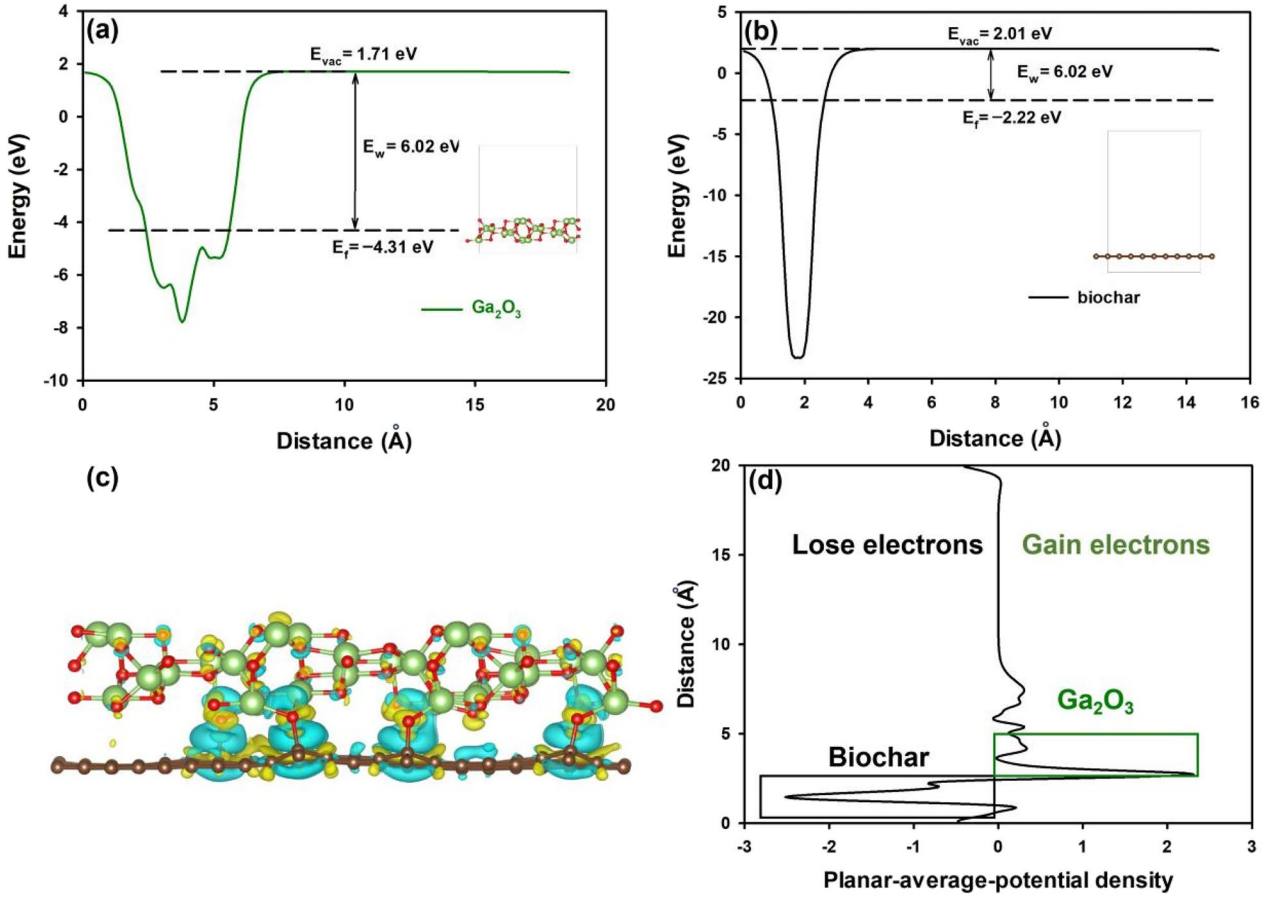

Fig. 3 Work function of **a** Ga_2O_3 and **b** biochar. **c** Differential charge and **d** charge density distribution along the c-axis direction at the Ga_2O_3/biochar interface. Blue and yellow regions represent electron depletion and accumulation, respectively

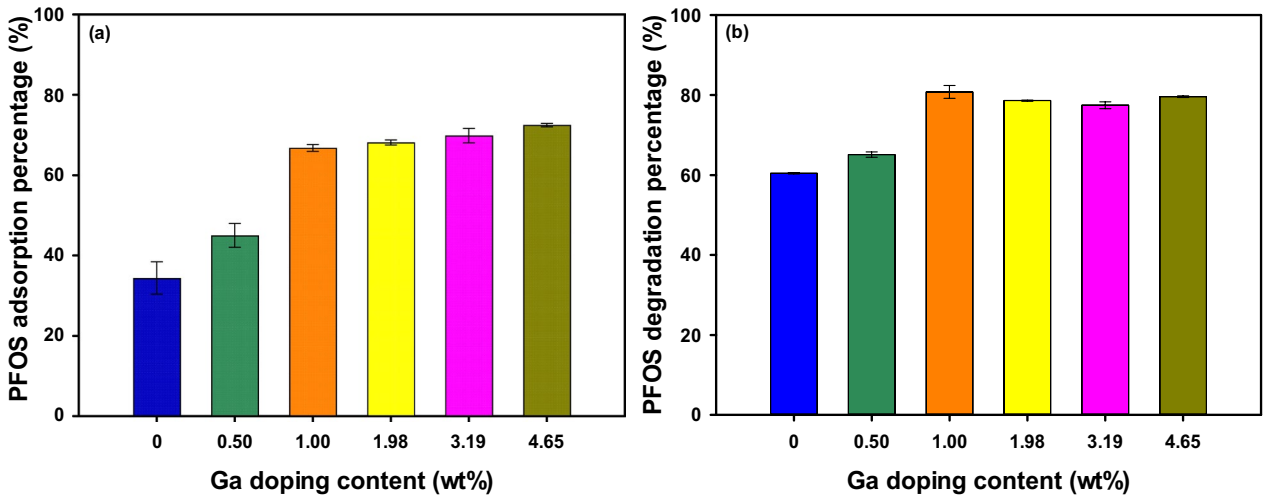

Fig. 4 **a** Effects of Ga content on PFOS adsorption by Ga_2O_3@biochar. Experimental conditions: initial PFOS = 100 μg L^{-1}, material dosage = 0.05 g L^{-1}, solution volume = 40 mL, pH = 7.0 ± 0.3, and reaction time = 24 h. **b** Effects of Ga content on photodegradation of preadsorbed PFOS by Ga_2O_3@biochar. Experimental conditions: Adsorption: initial PFOS concentration = 100 μg L^{-1}, solution volume = 40 mL, material dosage = 0.15 g L^{-1}, pH = 7.0 ± 0.3, and reaction time = 24 h; Photodegradation: UV intensity = 30 mW cm^{-2}, solution volume = 10 mL, pH = 7.0 ± 0.3, and reaction time = 8 h. Data plotted as the mean of triplicates and error bars refer to standard deviation

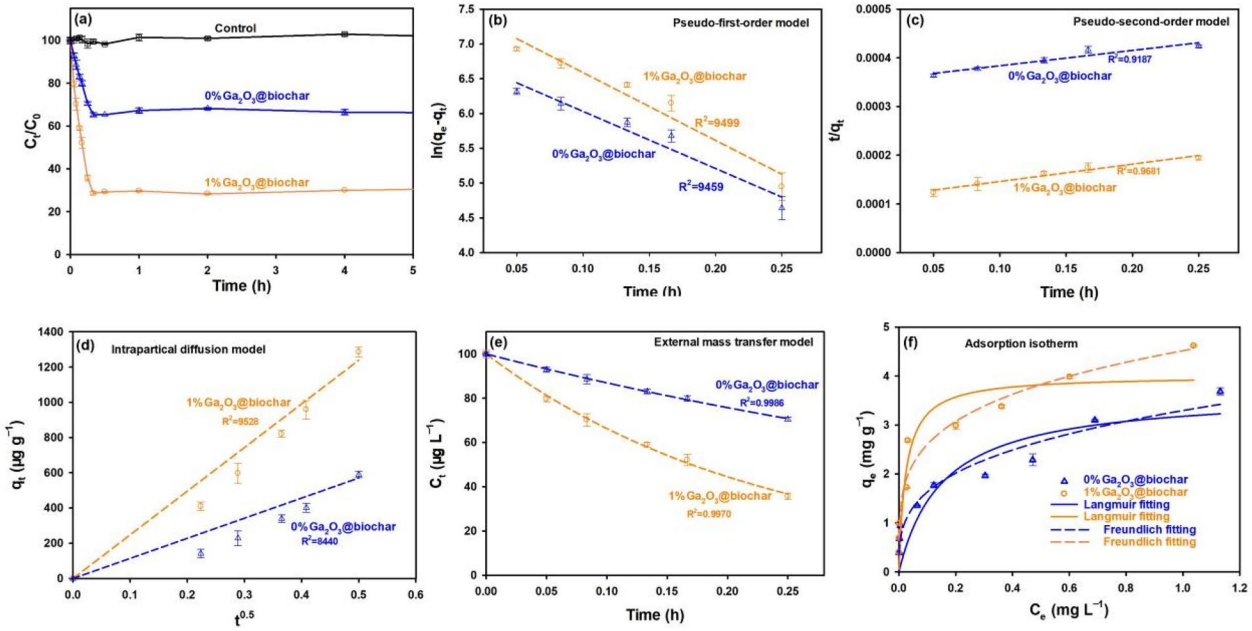

Fig. 5 **a** PFOS adsorption kinetics by Ga_2O_3@biochar, **b** pseudo first-order, **c** pseudo-second-order, **d** intraparticle diffusion, and **e** external mass transfer model fittings to the PFOS adsorption kinetic data. Experimental conditions: initial PFOS = 100 μg L^{-1}, material dosage = 0.05 g L^{-1}, solution volume = 40 mL, reaction time = 12 h, pH = 7.0 ± 0.3, and temperature = 23 ± 2 °C. **f** PFOS adsorption isotherms with Ga_2O_3@biochar. Experimental conditions: initial concentration PFOS = 0–1.5 mg L^{-1}, material dosage = 0.10 g L^{-1}, solution volume = 40 mL, reaction time = 24 h, pH = 7.0 ± 0.3, and temperature = 23 ± 2 °C. Data plotted as mean of triplicates and error bars refer to the standard deviation

cannot adsorb aqueous PFOS, while 0%Ga_2O_3@biochar at 0.05 g L^{-1} removed 34.4% of 100 μg L^{-1} PFOS within 24 h. The introduction of 1.0% Ga markedly increased the PFOS removal efficiency to 66.8%. Further increasing the Ga loading to 4.65% did not yield a statistically significant enhancement in PFOS removal (p-value = 0.29). The enhanced PFOS removal with Ga incorporation can be attributed to a synergistic interplay of multiple cooperative adsorption mechanisms, including hydrogen bonding, hydrophobic interaction, mesopore filling, and electrostatic attraction (see Sect. 3.4).

After reaching adsorption equilibrium under conditions of 100 μg L^{-1} initial PFOS and 0.15 g L^{-1} adsorbent (achieving 99% PFOS removal), the photodegradation of pre-concentrated PFOS on Ga_2O_3@biochar was evaluated following 8 h of UV irradiation (Fig. 4b). Increasing the Ga loading from 0 to 1.0% increased the PFOS photodegradation from 60.4% to 80.8%. It is noteworthy that 0%Ga_2O_3@biochar was able to photodegrade nearly 60% of PFOS due to its photoactive properties (Fig. 2). The incorporation of Ga facilitated light absorption and electron transfer and inhibited recombination of photogenerated electron–hole pairs (Sect. 3.1). However, when the Ga loading was further increased to 1.98%, 3.19%, and 4.65%, the PFOS photodegradation remained about the same. This can be attributed to (1) potential agglomeration of Ga_2O_3 at higher loadings, compromising the material synergies between biochar and Ga_2O_3, (2) weakened light harvesting ability and hindered photon utilization, and (3) excessive Ga may serve as e–h recombination centers (Wei et al. 2017; Zhu et al. 2021).

Considering both the PFOS adsorption and photodegradation efficiency, the optimal Ga doping was determined to be 1.0%, and thus 1%Ga_2O_3@biochar was further tested in the subsequent experiments.

3.4 Adsorption kinetics, isotherm, and mechanisms

Figure 5a compares the PFOS adsorption kinetics by 0%Ga_2O_3@biochar and 1%Ga_2O_3@biochar. PFOS adsorption proceeded rapidly, reaching equilibrium within 30 min. This fast kinetics is attributed to the efficient PFOS transport from the liquid phase to highly accessible active sites (Bai et al. 2020). Upon equilibrium, 1%Ga_2O_3@biochar removed 66.8% of PFOS, which nearly doubles that by 0%Ga_2O_3@biochar (34.4%), indicating a strong material synergy between biochar and Ga_2O_3 in promoting the PFOS uptake.

The pseudo-first-order (Eq. S1), pseudo-second-order (Eq. S2), intraparticle diffusion (Eq. S3), and film-diffusion-controlled kinetic models (Eq. S4) were employed to fit the adsorption kinetic data (Fig. 4b–e; Table S2). For

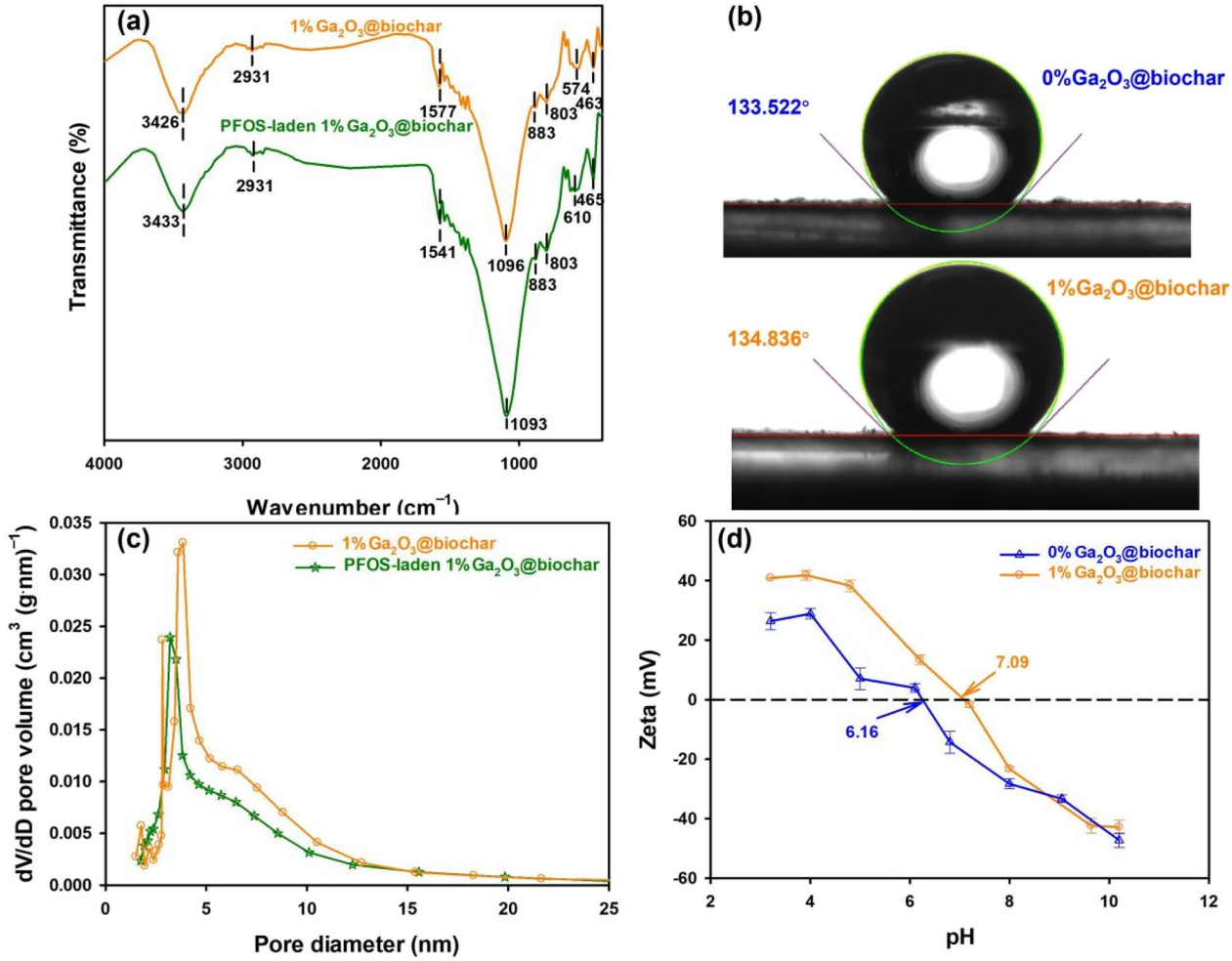

Fig. 6 **a** FTIR spectra, **b** contact angle, **c** pore size distribution, and **d** zeta potential of virgin and PFOS-laden 1%Ga_2O_3@biochar as well as 0%Ga_2O_3@biochar

0%Ga_2O_3@biochar, the pseudo-first-order model provided a better fit (R^2 = 0.946) than the pseudo-second-order model (R^2 = 0.919). For 1%Ga_2O_3@biochar, the pseudo-second-order model (R^2 = 0.968) offered a better fit than the pseudo-first-order model (R^2 = 0.950). The film diffusion model well simulated the kinetic data for both materials, implying that the film diffusion was likely the rate-limiting step.

Figure 5f compares the adsorption isotherms of PFOS by 0%Ga_2O_3@biochar and 1%Ga_2O_3@biochar. The experimental data were fitted with Langmuir (Eq. S11) and Freundlich (Eq. S12) isotherm models. The Freundlich model yielded a better fitting (R^2 = 0.956 for 0%Ga_2O_3@biochar and 0.962 for 1%Ga_2O_3@biochar) (Table S3), suggesting heterogeneous adsorption sites.

Figure 6a shows the FTIR spectra of 1%Ga_2O_3@biochar before and after PFOS adsorption. The –OH stretching band at 3426 cm^{-1} slightly shifted to 3433 cm^{-1} upon PFOS adsorption, which can be ascribed to hydrogen bonding between the sulfonate groups of PFOS and surface hydroxyl groups (Liu et al. 2024). The C=O stretching vibration at ~1577 cm^{-1} shifted to ~1541 cm^{-1} with reduced intensity, potentially arising from electrostatic interactions between the $–SO_3^-$ group and the positively charged surface of 1%Ga_2O_3@biochar (Zhang et al. 2021a).

Hydrophobic interaction has been known to play a critical role in adsorption of long-chain PFAS including PFOS by carbonaceous materials. The contact angles of 0%Ga_2O_3@biochar and 1%Ga_2O_3@biochar were measured to be 133.53° and 134.83° (Fig. 6b), respectively, demonstrating decent hydrophobicity of the biochar and that the Ga loading did not significantly affect the surface hydrophobicity. Therefore, while Ga_2O_3 greatly facilitated the PFOS adsorption, hydrophobic interaction between

PFOS and the carbonaceous surface of the biochar still played an important role (Mohd Jais et al. 2024).

The large specific surface area and porous structures of 1%Ga_2O_3@biochar (Table S4; Fig. 6c) provide abundant sorption sites for PFOS. Moreover, the dominance of mesopores (2–50 nm) and the large mesopore volume (0.15 $cm^3\ g^{-1}$) (Table S4) were conducive to intraparticle diffusion of PFOS (Du et al. 2016; Liu et al. 2023) and elevated sorption capacity through the pore-filling mechanism (Liu et al. 2023). Upon PFOS adsorption, the specific surface area was decreased from 276.7 to 43.8 $m^2\ g^{-1}$, and the pore volume from 0.23 to 0.10 $cm^3\ g^{-1}$. Moreover, the bimodal pore volume distribution with two peaks at 2.82 and 3.85 nm turned into a monomodal distribution with one peak at 3.20 nm. Taken together, these observations suggest that a multilayer PFOS adsorption or hole filling mechanism was operative within the mesopores (Pauletto et al. 2023).

The pH of point of zero charge (pH_{PZC}) of 0%Ga_2O_3@biochar and 1%Ga_2O_3@biochar was determined to be 6.16 and 7.09, respectively (Fig. 6d). Under the experimental conditions (pH = 7.0 ± 0.2), 0%Ga_2O_3@biochar was negatively charged while 1%Ga_2O_3@biochar was positively charged. Therefore, 1%Ga_2O_3@biochar offered a more favorable PFOS adsorption through electrostatic attraction (Tang et al. 2010).

Taken together, the superior PFOS adsorption by 1%Ga_2O_3@biochar arises from a synergistic interplay of multiple cooperative adsorption mechanisms: (1) hydrogen bonding involving oxygen containing functional groups of 1%Ga_2O_3@biochar (i.e., –OH) and sulfonate moieties of PFOS, (2) hydrophobic interactions between hydrophobic PFOS and the hydrophobic composite, (3) pore filling within the well-developed mesoporous structure, and (4) electrostatic attraction between positively charged surface sites and anionic PFOS.

3.5 Photocatalytic degradation of pre-concentrated PFOS on Ga_2O_3@biochar

Figure 7 shows the photocatalytic degradation kinetics of PFOS pre-concentrated on 0%Ga_2O_3@biochar and 1%Ga_2O_3@biochar under UV irradiation. After 8 h of reaction, the PFOS degradation efficiencies reached 60.4% and 80.8%, respectively (Fig. 7a).

The pseudo-first-order (Eq. S13) and retarded-first-order kinetic models (Eq. S14; Text S6) were employed to fit the degradation kinetics data. The latter model, which incorporates a retardation factor (α) into the reaction rate constant, provided a superior fitting ($R^2 = 0.994$ for 0%Ga_2O_3@biochar and $R^2 = 0.998$ for 1%Ga_2O_3@biochar) (Fig. 7b, c; Table S5). The observation reveals some important processes during the photodegradation, including (1) weakening reactivity of PFOS at active sites over time, (2) increasing diffusion limitation as reactive sites became less accessible, (3) competitive adsorption and reaction of the intermediate products, and (4) delayed generation of ROS.

Defluorination analysis further corroborated the enhanced performance of 1%Ga_2O_3@biochar. The defluorination efficiency after 8 h reached 70.5% for 1%Ga_2O_3@biochar, far exceeding the 50.0% defluorination for 0%Ga_2O_3@biochar. The remaining fluorine fraction was inferred to reside within the residual parent PFOS and the qualitatively identified shorter-chain intermediates (Sect. 3.6). This remarkable enhancement distinctly benefited from the unique structural and optoelectronic advantages of the composite, specifically its accommodating mesoporosity and highly efficient interfacial charge separation. Notably, the composite exhibited considerably higher degradation and defluorination efficiencies than most previously reported photocatalysts (Table S6), highlighting its strong potential for efficient PFOS destruction and deep mineralization.

3.6 Mechanistic insights into PFOS photodegradation

To elucidate the reactive species involved in PFOS photodegradation, radical quenching experiments were conducted using specific scavengers: EDTA-2Na for h^+, $AgNO_3$ for e^-, IPA for ·OH, BQ for $\cdot O_2^-$, and FFA for $^1O_2$. As illustrated in Fig. 8a, the addition of $AgNO_3$, BQ, and FFA inhibited the PFOS degradation from 80.8% to 53.5%, 42.2%, and 61.6%, respectively, underscoring the critical roles of e^-, $\cdot O_2^-$, and $^1O_2$ in the degradation process. The addition of EDTA-2Na and IPA exhibited negligible effects, implying insignificant roles of h^+ and ·OH. The ESR data provided direct evidence for the generation of $\cdot O_2^-$ and $^1O_2$ under the UV irradiation (Fig. 8b). A characteristic quartet signal with an intensity ratio of 1:1:1:1 for DMPO-$\cdot O_2^-$ verified the formation of $\cdot O_2^-$ (Chen et al. 2021), and a characteristic spectrum with an intensity ratio of 1:1:1 indicated the generation of $^1O_2$ (Hoebeke et al. 1997). Moreover, the presence of $AgNO_3$, BQ, and FFA decreased the pseudo-first-order rate constant (k) from 0.233 to 0.089, 0.104, and 0.138 h^{-1}, respectively (Fig. 8c; Fig. S4; Table S7). Based on these results, the relative contributions of e^-, $\cdot O_2^-$, and $^1O_2$ to PFOS photodegradation were estimated to be 35.0%, 39.1%, and 25.8%, respectively.

The intermediates generated during PFOS photodegradation were elucidated following an 8 h period of UV exposure (Fig. S5) and are summarized in Table S8. Perfluorooctanoic acid (PFOA), perfluoroheptanoic acid (PFHpA), perfluorohexanoic acid (PFHxA), perfluoropentanoic acid (PFPeA), and perfluorobutanoic acid

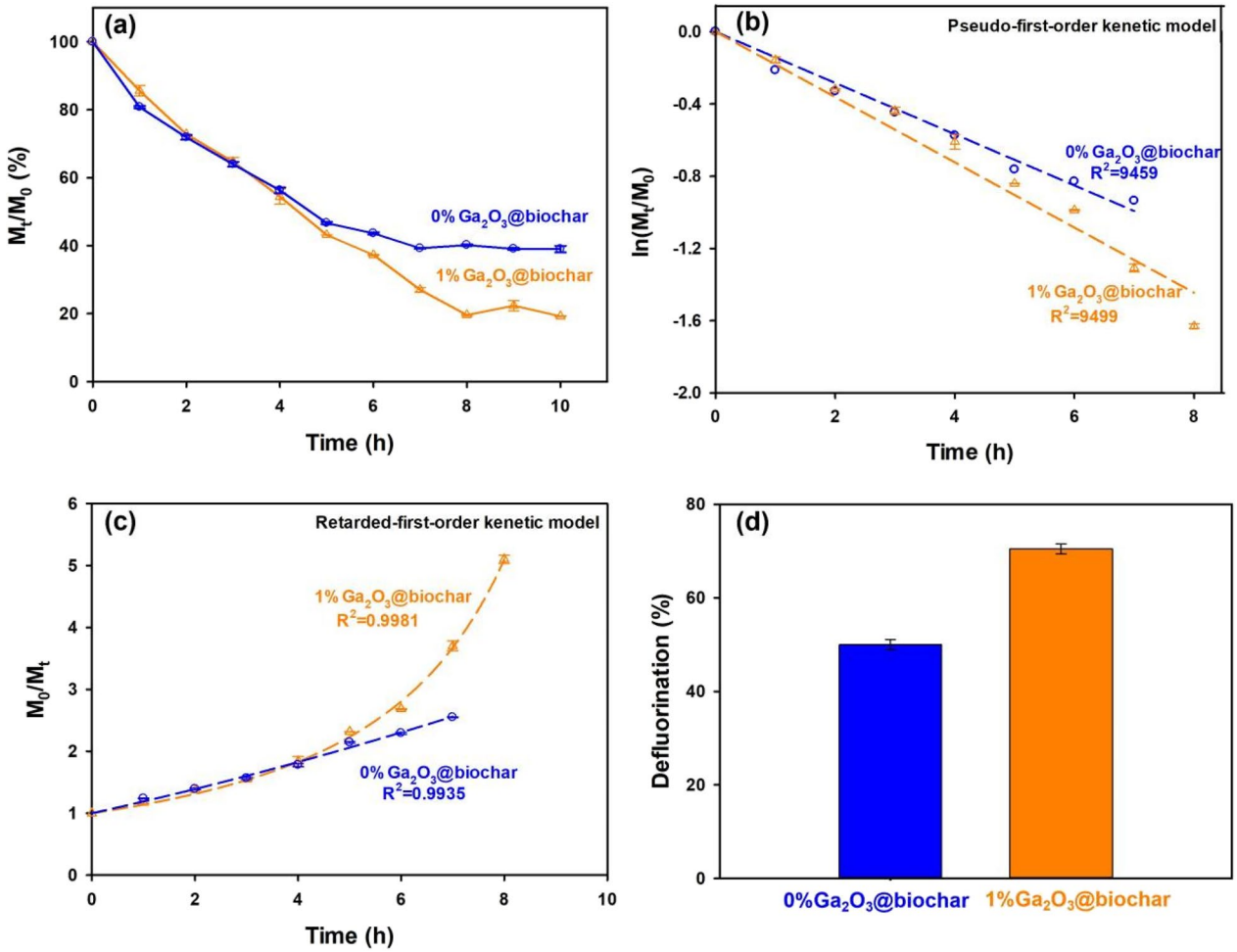

Fig. 7 **a** Photodegradation kinetics of pre-adsorbed PFOS on 0%Ga_2O_3@biochar and 1%Ga_2O_3@biochar; **b** pseudo-first-order and **c** retarded-first-order kinetic model fittings to the experimental degradation data; and **d** defluorination percentage of pre-adsorbed PFOS on Ga_2O_3@biochar. Experimental conditions: initial pre-adsorbed PFOS quantity = 666.7 μg g^{-1}, material dosage = 0.60 g L^{-1}, solution volume = 10 mL, pH = 7.0 ± 0.3, temperature = 23 ± 2 °C, reaction time = 8 h, UV wavelength = 254 nm, and light intensity = 30.0 mW cm^{-2}

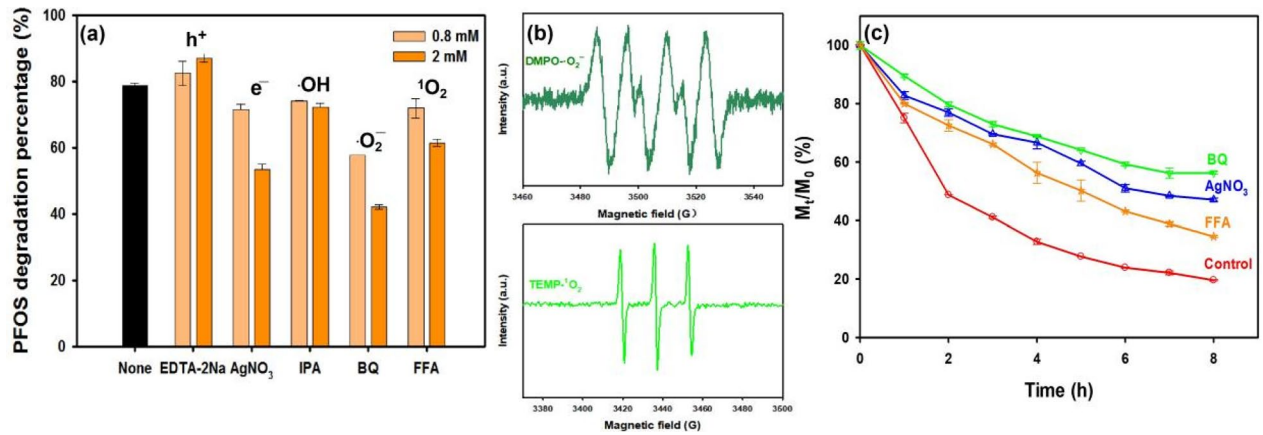

Fig. 8 **a** Effects of various scavengers on photodegradation of pre-concentrated PFOS onto 1%Ga_2O_3@biochar, **b** electron spin resonance (ESR) spectra of 1%Ga_2O_3@biochar, and **c** effects of various scavengers on photodegradation kinetics of pre-concentrated PFOS onto 1%Ga_2O_3@biochar

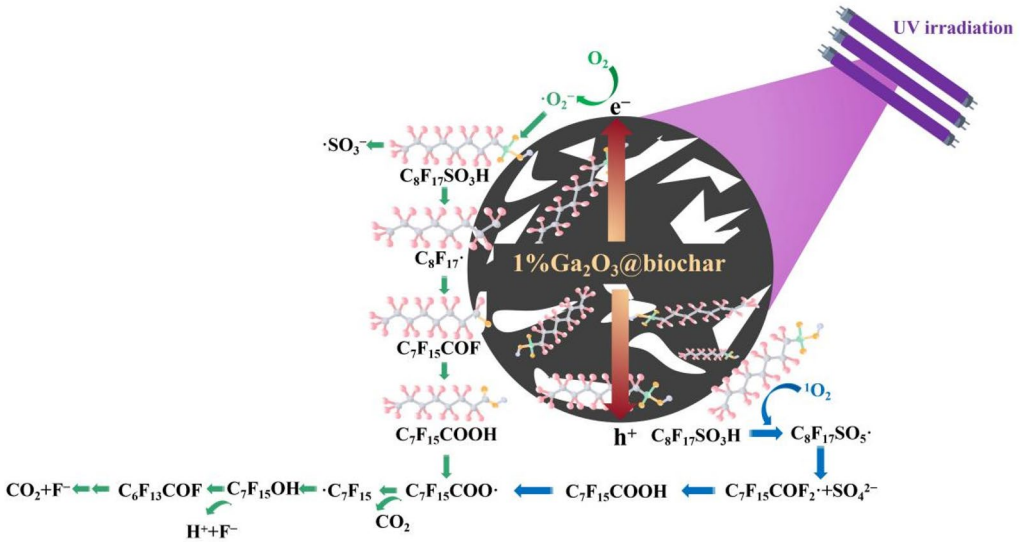

Fig. 9 Conceptualized illustration of photocatalytic reaction mechanisms of PFOS by 1%Ga_2O_3@biochar

(PFBA) were detected, all of which exhibit lower toxicities compared to the parent PFOS (Table S9).

Accordingly, two plausible primary photodegradation pathways for pre-concentrated PFOS by 1%Ga_2O_3@biochar are proposed (Fig. 9). First, e^- and $\cdot O_2^-$ mediated degradation: Under UV irradiation, electrons (e^-) and holes (h^+) are generated (Eq. 2). The photogenerated electrons react with O_2 to form $\cdot O_2^-$ (Eq. 3). The resulting $\cdot O_2^-$ attacks PFOS, leading to the formation of an unstable perfluorooctyl radical (C_8F_{17}) (Eq. 4). $C_8F_{17}\cdot$ subsequently goes through hydrolysis, yielding $C_7F_{15}COF$ and F^- (Eqs. 5, 6). Further hydrolysis of $C_7F_{15}COF$ produces PFOA (Eq. 7). Through sequential $\cdot O_2^-$-driven decarboxylation and defluorination, PFOA is further degraded into shorter-chain PFCAs, ultimately achieving complete mineralization (Zhu et al. 2021).

$$1\%Ga_2O_3@biochar + hv \rightarrow e^- + h^+ \quad (2)$$

$$e^- + O_2 \rightarrow \cdot O_2^- \quad (3)$$

$$\cdot O_2^- + C_8F_{17}SO_3^- \rightarrow C_8F_{17}\cdot + SO_3^- \quad (4)$$

$$C_8F_{17}\cdot + H_2O \rightarrow C_8F_{17}OH + H^+ \quad (5)$$

$$C_8F_{17}OH \rightarrow C_7F_{15}COF + H^+ + F^- \quad (6)$$

$$C_7F_{15}COF + H_2O \rightarrow C_7F_{15}COOH + H^+ + F^- \quad (7)$$

$$C_7F_{15}COO^- + \cdot O_2^- \rightarrow \cdot C_7F_{15} + COO^- \quad (8)$$

Second, $^1O_2$ mediated degradation: Direct electron transfer between $^1O_2$ and PFOS results in an unstable intermediate $C_8F_{17}SO_5\cdot$, which undergoes intramolecular rearrangement to form $C_7F_{15}COF_2\cdot$ (Eq. 11). $C_7F_{15}COF_2\cdot$ is subsequently hydrolyzed to yield PFOA (Eq. 12) (Jiang et al. 2023). The resulting PFOA undergoes the stepwise defluorination and chain-shortening reactions via mechanisms analogous to those described in Pathway I.

$$\cdot O_2^- + H^+ \rightarrow HO_2\cdot \quad (9)$$

$$2HO_2\cdot \rightarrow {}^1O_2 + H_2O_2 \quad (10)$$

$$C_8F_{17}SO_3^- + {}^1O_2 \rightarrow C_8F_{17}SO_5 \rightarrow C_7F_{15}COF_2\cdot + SO_4^{2-} \quad (11)$$

$$C_7F_{15}COF_2\cdot + H_2O \rightarrow C_7F_{15}COOH + H^+ + F^- \quad (12)$$

3.7 Reusability and post-reaction stability of Ga_2O_3@biochar

To evaluate the practical applicability and durability of 1%Ga_2O_3@biochar, the composite was subjected to four sequential adsorption–photodegradation cycles (Fig. S6). 1%Ga_2O_3@biochar retained excellent adsorption performance with PFOS removal efficiencies consistently exceeding 99.0% across all cycles, highlighting the high stability of the biochar-based matrix. However, the photodegradation efficiency experienced a gradual decline, reaching ~50% after the fourth cycle. Post-reaction XRD and FTIR analyses (Fig. S7) were conducted to evaluate

the structural integrity of the composite. The retention of characteristic diffraction peaks and the persistence of oxygen-containing functional groups confirmed that the material was chemically and physically resilient under intense UV irradiation. Consequently, the observed decline in photodegradation was likely not due to structural collapse, but rather the competitive occupancy of reactive sites by recalcitrant intermediate products and a subsequent reduction in ROS generation and/or accessibility via surface passivation. Notably, the photocatalytic process regenerated the composite by degrading pre-adsorbed PFOS, representing a major advantage of the adsorptive photocatalyst over conventional adsorbents, whose regeneration often requires expensive and toxic chemicals and solvents.

3.8 Concentration and destruction of PFOS in real groundwater using 1%Ga_2O_3@biochar

The performance of 1%Ga_2O_3@biochar for PFOS concentration and destruction was further evaluated under real groundwater matrix conditions. As shown in Fig. S8, the composite exhibited excellent adsorption ability, with more than 99% PFOS adsorbed within 30 min. However, the photocatalytic degradation efficiency of PFOS declined in the groundwater matrix, reaching only 57.5%, a 25.0% reduction compared to that with deionized water. This observation revealed notable interference of the complex groundwater compositions (Table S10), in particular, total organic carbon (1.9 mg L^{-1}), which may shield against UV irradiation, compete for photoinduced electrons, and scavenge ROS (Wang et al. 2019).

4 Conclusions

In this study, we prepared and tested a β-Ga_2O_3-functionalized biochar composite (Ga_2O_3@biochar) for efficient PFOS degradation and mineralization via a synergistic concentrate-and-destroy strategy. The incorporation of β-Ga_2O_3 into the porous structure of biochar modulated its physicochemical and optoelectronic properties, resulting in enhanced mesoporosity for improved PFOS diffusion and sorption, improved light absorption, reduced bandgap, and suppressed recombination of photogenerated electron–hole pairs. The composite at a Ga loading of 1% (1%Ga_2O_3@biochar) exhibited the highest adsorption and most effective photodegradation of PFOS. More than 99% of PFOS was adsorbed within 30 min. Subsequently, 80.8% of the pre-sorbed PFOS was degraded in 8 h under UV irradiation, with 70.5% defluorinated. The enhanced adsorption stemmed from synergy of multiple mechanisms including hydrogen bonding, hydrophobic interaction, mesopore filling, and electrostatic attraction. In addition to the much improved material property and the preconcentrating effect, e^-, $\cdot O_2^-$, and $^1O_2$ played important roles, with relative contributions of 35.0%, 39.1%, and 25.8% to the overall PFOS degradation, respectively. The PFOS degradation followed the stepwise chain-shortening mechanism. The composite maintained excellent adsorption capacity and photocatalytic activity over four adsorption–photodegradation cycles. Preliminary data also revealed that the material can potentially effectively adsorb and degrade PFOS under real groundwater conditions despite some notable water matrix interference. Overall, 1%Ga_2O_3@biochar appeared to be a promising adsorptive photocatalyst, which may enable the concentrate-&-destroy strategy for treating PFOS and likely other PFAS in water. Future studies can focus on (1) elucidating the influence of complex environmental conditions (i.e., dissolved organic matter, pH, coexisting ions, and light conditions) on PFOS adsorption and photodegradation, (2) comprehensive identification and toxicity assessment of degradation byproducts, (3) pilot-scale validation under environmentally relevant conditions, (4) life cycle assessment to quantify the environmental impact and assess economic viability of the technology, and (5) expanding the applicability to other PFAS.

Supplementary Information

The online version contains supplementary material available at https://doi.org/10.1007/s42773-026-00642-8.

Additional file 1.

Author contributions

Data curation, formal analysis, investigation, methodology, and validation were performed by Dongjiao Lin. Methodology, investigation, and data curation were performed by Ying Liu. Software and formal analysis were carried out by Shuai Gao and Haodong Ji. Writing—review & editing were carried out by Lianjun Bao, Honghong Lyu, and Dongye Zhao. Formal analysis was performed by Zuhui Wu. Conceptualization, methodology, resources, writing—original draft, writing-review & editing, supervision, project administration, and funding acquisition were performed by Yanyan Gong. The authors read and approved the final manuscript.

Funding

The authors gratefully acknowledge the partial financial supports from National Natural Science Foundation of China (42577249 and 42177186), Guangzhou Basic and Applied Basic Research Foundation (2025A04J0991), Guangdong Key Laboratory of Environmental Pollution and Health (2016B030301005), the US Strategic Environmental Research and Development Program (ER18-1515), and the US National Science Foundation (CBET-2244985).

Data availability

Data will be made available upon request.

Declarations

Competing interests

The authors declare that they have no known competing financial interests or personal relationships that could have appeared to influence the work reported in this paper.

Author details
[1]College of Environment and Climate, Guangdong Provincial Key Laboratory of Environmental Pollution and Health, Jinan University, Guangzhou 511443, People's Republic of China. [2]Eco-Environment and Resource Efficiency Research Laboratory, School of Environment and Energy, Peking University Shenzhen Graduate School, Shenzhen 518055, People's Republic of China. [3]Tianjin Key Laboratory of Clean Energy and Pollution Control, School of Energy and Environmental Engineering, Hebei University of Technology, Tianjin 300401, People's Republic of China. [4]Department of Civil, Construction and Environmental Engineering, San Diego State University, San Diego, CA 92182-1324, USA.

Received: 27 February 2026 Revised: 19 May 2026 Accepted: 1 June 2026
Published online: 26 June 2026

References

Bai Y, Wu F, Gong Y (2020) Oxidation and adsorption of antimony (III) from surface water using novel Al_2O_3-supported Fe–Mn binary oxide nanoparticles: effectiveness, dynamic quantitative mechanisms, and life cycle analysis. Environ Sci Nano 7(10):3047–3061

Barzen-Hanson KA, Roberts SC, Choyke S, Oetjen K, McAlees A, Riddell N, McCrindle R, Ferguson PL, Higgins CP, Field JA (2017) Discovery of 40 classes of per- and polyfluoroalkyl substances in historical aqueous film-forming foams (AFFFs) and AFFF-Impacted groundwater. Environ Sci Technol 51(4):2047–2057

Chen Y, Lan S, Zhu M (2021) Construction of piezoelectric $BaTiO_3/MoS_2$ heterojunction for boosting piezo-activation of peroxymonosulfate. Chin Chem Lett 32(6):2052–2056

Du Z, Deng S, Bei Y, Huang Q, Wang B, Huang J, Yu G (2014) Adsorption behavior and mechanism of perfluorinated compounds on various adsorbents—a review. J Hazard Mater 274:443–454

Du Z, Deng S, Liu D, Yao X, Wang Y, Lu X, Wang B, Huang J, Wang Y, Xing B, Yu G (2016) Efficient adsorption of PFOS and F53B from chrome plating wastewater and their subsequent degradation in the regeneration process. Chem Eng J 290:405–413

Fu CX, Xu XR, Zheng CM, Liu XJ, Zhao DD, Qiu WH (2022a) Photocatalysis of aqueous PFOA by common catalysts of In_2O_3, Ga_2O_3, TiO_2, CeO_2 and CdS: influence factors and mechanistic insights. Environ Geochem Health 44(9):2943–2953

Fu SY, Zhang Y, Xu XY, Dai X, Zhu L (2022b) Peroxymonosulfate activation by iron self-doped sludge-derived biochar for degradation of perfluorooctanoic acid: a singlet oxygen-dominated nonradical pathway. Chem Eng J 450:137953

Gagliano E, Sgroi M, Falciglia PP, Vagliasindi FGA, Roccaro P (2020) Removal of poly- and perfluoroalkyl substances (PFAS) from water by adsorption: role of PFAS chain length, effect of organic matter and challenges in adsorbent regeneration. Water Res 171:115381

Gonzalez-Gonzalez RB, Parra-Saldivar R, Alsanie WF, Iqbal HMN (2022) Nanohybrid catalysts with porous structures for environmental remediation through photocatalytic degradation of emerging pollutants. Environ Res 214(Pt 2):113955

Habib Z, Song M, Ikram S, Zahra Z (2024) Overview of per- and polyfluoroalkyl substances (PFAS), their applications, sources, and potential impacts on human health. Pollutants 4(1):136–152

Hoebeke M, Schuitmaker HJ, Jannink LE, Dubbelman TM, Jakobs A, Van de Vorst A (1997) Electron spin resonance evidence of the generation of superoxide anion, hydroxyl radical and singlet oxygen during the photohemolysis of human erythrocytes with bacteriochlorin a. Photochem Photobiol 66(4):502–508

Jia L, Yu Y, Li ZP, Qin SN, Guo JR, Zhang YQ, Wang JC, Zhang JC, Fan BG, Jin Y (2021) Study on the Hg(0) removal characteristics and synergistic mechanism of iron-based modified biochar doped with multiple metals. Bioresour Technol 332:125086

Jiang Y, Hu Y, Yu Z, Lv Y, Liu Y, Li X, Lin C, Ye X, Yang G, Liu M (2023) Rapid PFOS mineralization with peroxydisulfate activation process mediated by N modified Fe-based catalyst. Ecotoxicol Environ Saf 263:115364

Li F, Duan J, Tian S, Ji H, Zhu Y, Wei Z, Zhao D (2020) Short-chain per- and polyfluoroalkyl substances in aquatic systems: occurrence, impacts and treatment. Chem Eng J 380:122506

Lin DJ, Lyu H, Liu YJ, Gong YY (2025) Rapid and efficient removal of aqueous perfluorooctane sulfonate at environmentally relevant concentrations using photoregenerable modified biochar. Chem Eng J 523:168638

Liu FQ, Guan XH, Xiao F (2022) Photodegradation of per- and polyfluoroalkyl substances in water: a review of fundamentals and applications. J Hazard Mater 439:129580

Liu Z, Zhang P, Wei Z, Xiao F, Liu S, Guo H, Qu C, Xiong J, Sun H, Tan W (2023) Porous Fe-doped graphitized biochar: an innovative approach for co-removing per-/polyfluoroalkyl substances with different chain lengths from natural waters and wastewater. Chem Eng J 476:146888

Liu ZZ, Pan CG, Peng FJ, Hu JJ, Tan HM, Zhu RG, Zhou CY, Liang H, Yu K (2024) Rapid adsorptive removal of emerging and legacy per- and polyfluoroalkyl substances (PFASs) from water using zinc chloride-modified litchi seed-derived biochar. Bioresour Technol 408:131157

Liu Y, Liu Y, Zhang A, Yang C, Wang Y, Zhou H, Yang S, Tang J, Sun J, Liu Y (2025) Behavior and mechanism of perfluorooctane sulfonate (PFOS) removal from wastewater samples using bamboo powder biochar. J Water Process Eng 70:107102

Loos R, Gawlik BM, Locoro G, Rimaviciute E, Contini S, Bidoglio G (2009) EU-wide survey of polar organic persistent pollutants in European river waters. Environ Pollut 157(2):561–568

Luo K, Pang Y, Wang D, Li X, Wang L, Lei M, Huang Q, Yang Q (2021) A critical review on the application of biochar in environmental pollution remediation: role of persistent free radicals (PFRs). J Environ Sci 108:201–216

Lv M, Zhang X, Li B, Huang B, Zheng Z (2024) Single-particle fluorescence spectroscopy for elucidating charge transfer and catalytic mechanisms on nanophotocatalysts. ACS Nano 18(44):30247–30268

Meng L, Yin W, Wang S, Wu X, Hou J, Yin W, Feng K, Ok YS, Wang X (2020) Photocatalytic behavior of biochar-modified carbon nitride with enriched visible-light reactivity. Chemosphere 239:124713

Mohd Jais F, Ibrahim MSI, El-Shafie A, Choong CE, Kim M, Yoon Y, Jang M (2024) Updated review on current approaches and challenges for poly- and perfluoroalkyl substances removal using activated carbon-based adsorbents. J Water Process Eng 64:105625

Pan X, Wang X, Zhang Z, Ma C, Chen J, Yuan Y, Li H (2025) S-scheme γ-Ga_2O_3/CdS heterojunction with good photocatalytic overall water splitting performance. J Alloys Compd 1013:178595

Pauletto PS, Florent M, Bandosz TJ (2023) On the directions of carbon surface modifications towards efficient PFOS removal: analyzing the interplay of porosity and surface chemistry. Chem Eng J 455:140897

Perdew JP, Burke K, Ernzerhof M (1996) Generalized gradient approximation made simple. Phys Rev Lett 77(18):3865

Ramos P, Ashworth DJ (2024) Per- and poly-fluoroalkyl substances in agricultural contexts and mitigation of their impacts using biochar: a review. Sci Total Environ 927:172275

Ruiz-Vargas J, Siredey-Schwaller N, Noyrez P, Mathieu S, Bocher P, Gey N (2014) Potential and limitations of microanalysis SEM techniques to characterize borides in brazed Ni-based superalloys. Mater Charact 94:46–57

Su X, Wang XM, Ge ZY, Bao ZR, Lin L, Chen YX, Dai WN, Sun YY, Yuan HC, Yang W, Meng J, Wang HL, Pillai SC (2024) KOH-activated biochar and chitosan composites for efficient adsorption of industrial dye pollutants. Chem Eng J 486:150387

Tang CY, Shiang FuQ, Gao D, Criddle CS, Leckie JO (2010) Effect of solution chemistry on the adsorption of perfluorooctane sulfonate onto mineral surfaces. Water Res 44(8):2654–2662

United States Environmental Protection Agency (2025) Per- and polyfluoroalkyl substances (PFAS) final PFAS national primary drinking water regulation. https://www.epa.gov/sdwa/and-polyfluoroalkyl-substances-pfas. Accessed 20 Jan 2026

Wang F, Shih K (2011) Adsorption of perfluorooctanesulfonate (PFOS) and perfluorooctanoate (PFOA) on alumina: influence of solution pH and cations. Water Res 45(9):2925–2930

Wang JQ, Chen JW, Qiao XL, Zhang YN, Uddin M, Guo ZY (2019) Disparate effects of DOM extracted from coastal seawaters and freshwaters on photodegradation of 2,4-dihydroxybenzophenone. Water Res 151:280–287

Wang H, Teng H, Wang X, Xu J, Sheng L (2022) Physicochemical modification of corn straw biochar to improve performance and its application of constructed wetland substrate to treat city tail water. Environ Manag 310:114758
Wang Z, Lin X, Yang KLD, Lin D (2024) Differential photodegradation processes of adsorbed polychlorinated biphenyls on biochar colloids with various pyrolysis temperatures. Water Res 251:121174
Wee SY, Aris AZ (2023) Revisiting the "forever chemicals", PFOA and PFOS exposure in drinking water. Npj Clean Water 6(1):57
Wei JP, Yang J, Wen ZH, Dai J, Li Y, Yao BH (2017) Efficient photocatalytic oxidation of methane over β-Ga_2O_3/activated carbon composites. RSC Adv 7(60):37508–37521
Xiao F, Simcik MF, Halbach TR, Gulliver JS (2015) Perfluorooctane sulfonate (PFOS) and perfluorooctanoate (PFOA) in soils and groundwater of a U.S. metropolitan area: migration and implications for human exposure. Water Res 72:64–74
Xu T, Ji H, Gu Y, Tong T, Xia Y, Zhang L, Zhao D (2020) Enhanced adsorption and photocatalytic degradation of perfluorooctanoic acid in water using iron (hydr)oxides/carbon sphere composite. Chem Eng J 388:124230
Yu B, Man Y, Wang P, Wu C, Xie J, Wang W, Jiang H, Zhang L, Zhang Y, Mao L, Zhu L, Zheng Y, Liu X (2023) Catalytic degradation of dimethomorph by nitrogen-doped rice husk biochar. Ecotoxicol Environ Saf 257:114908
Zhang J, Jiang F, Zhang L (2004) Fabrication, structural characterization and optical properties of semiconducting gallium oxide nanobelts. Phys Lett A 322(5):363–368
Zhang J, Liu Z, Lin C, Lin J (2005) A simple method to synthesize β-Ga_2O_3 nanorods and their photoluminescence properties. J Cryst Growth 280(1):99–106
Zhang WL, Zhang DQ, Liang YN (2019) Nanotechnology in remediation of water contaminated by poly- and perfluoroalkyl substances: a review. Environ Pollut 247:266–276
Zhang D, He Q, Wang M, Zhang W, Liang Y (2021a) Sorption of perfluoroalkylated substances (PFASs) onto granular activated carbon and biochar. Environ Technol 42(12):1798–1809
Zhang K, Sun P, Khan A, Zhang Y (2021b) Photochemistry of biochar during ageing process: reactive oxygen species generation and benzoic acid degradation. Sci Total Environ 765:144630
Zhang Y, Tan X, Lu R, Tang Y, Qie H, Huang Z, Zhao J, Cui J, Yang W, Lin A (2023) Enhanced removal of polyfluoroalkyl substances by simple modified biochar: adsorption performance and theoretical calculation. ACS EST Water 3(3):817–826
Zhu Y, Xu T, Zhao D, Li F, Liu W, Wang B, An B (2021) Adsorption and solid-phase photocatalytic degradation of perfluorooctane sulfonate in water using gallium-doped carbon-modified titanate nanotubes. Chem Eng J 421:129676
Zhu Y, Leary RN III, Xu T, He K, Blaney L, Hao X, Zhao DY (2026) Photocatalytic degradation of PFAS under field water matrix conditions using an adsorptive photocatalyst. Water Res X 30:100485